Materials & Design 231 (2023) 112087

Contents lists available at ScienceDirect

Materials & Design

journal homepage: www.elsevier.com/locate/matdes

Osteoporosis and Covid-19: Detected similarities in bone lacunar-level alterations via combined AI and advanced synchrotron testing

Federica Buccino [a], Luigi Zagra [b], Elena Longo [c], Lorenzo D'Amico [c], Giuseppe Banfi [b], Filippo Berto [d,e], Giuliana Tromba [c], Laura Maria Vergani [a,*]

[a] Department of Mechanical Engineering, Politecnico di Milano, 20156, Italy
[b] I.R.C.C.S Ospedale Galeazzi - Sant'Ambrogio, Milano 20157, Italy
[c] Elettra-Sincrotrone Trieste SCpA, Basovizza, Trieste 34149, Italy
[d] Università La Sapienza, Rome 00185, Italy
[e] NTNU, Norway

HIGHLIGHTS

•The variability in trabecular bone features is due to the external loading scenario.•Osteoporosis signs start appearing at the micro-scale.•Covid-19 deteriorates micro-scale porosities.

GRAPHICAL ABSTRACT

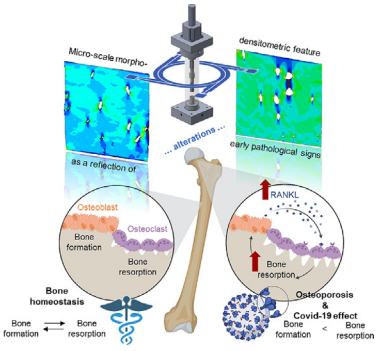

ARTICLE INFO

Article history:
Received 17 March 2023
Revised 3 May 2023
Accepted 9 June 2023
Available online 11 June 2023

Keywords:
Bone lacunae
Micro-scale
Synchrotron
Osteoporosis
Covid-19

ABSTRACT

While advanced imaging strategies have improved the diagnosis of bone-related pathologies, early signs of bone alterations remain difficult to detect. The Covid-19 pandemic has brought attention to the need for a better understanding of bone micro-scale toughening and weakening phenomena. This study used an artificial intelligence-based tool to automatically investigate and validate four clinical hypotheses by examining osteocyte lacunae on a large scale with synchrotron image-guided failure assessment. The findings indicate that trabecular bone features exhibit intrinsic variability related to external loading, micro-scale bone characteristics affect fracture initiation and propagation, osteoporosis signs can be detected at the micro-scale through changes in osteocyte lacunar features, and Covid-19 worsens micro-scale porosities in a statistically significant manner similar to the osteoporotic condition. Incorporating these findings with existing clinical and diagnostic tools could prevent micro-scale damages from progressing into critical fractures.

1. Introduction

Bone formation and resorption are vital biological processes performed by osteoblasts and osteoclasts, respectively, and are required to maintain bone homeostasis and guarantee bone defect

* Corresponding author at: Via La Masa 1, 20156 Milano, Italy.
E-mail address: laura.vergani@polimi.it (L.M. Vergani).

https://doi.org/10.1016/j.matdes.2023.112087
0264-1275/

healing. These activities are carefully orchestrated by osteocytes, mechanosensory cells that respond to mechanical loading, play an integral role in regulating bone regeneration, as well as engaging in perilacunar/canalicular remodeling [1-3]. Osteocyte cell bodies are embedded in micron-sized ellipsoidal pores ($\sim 20 \times 10 \times 5$ μm) named lacunae [4], that are interconnected through a dense network of canaliculi, slender long channels which diameters are ranging from 0.15 to 0.55 μm [5].

At the micro-scale, the evolution of damage into a macro-scale critical fracture is still an obscure point, specifically due to a lack in understanding the role of lacunae in bone micro-damage. Lacunae seem to play an antithetical mechanical function, having an effect on both strength and toughness. In the first instance, lacunae could be classified as stress concentrators [2,6]. The average tissue strain around lacunae is 1.5–4.5 times higher than the remote strain applied to the surrounding tissue, so, lacunar system should contribute to strength decreases. Indeed, experimentally measured bone matrix strains around osteocyte lacunae can reach peaks in strain concentration factor of 1.1–3.8 with respect to the remote tissue strain, highly influencing crack patterns around the perilacunar regions [7]. However, considering bone as a damage-tolerant material [8,9], meaning that it is able to tolerate the presence of microcracks without reaching the level of critical size defects, lacunae are able to deviate the crack path, slowing down damage progression. Toughening phenomena are also visible at the nano-scale, where bone could become insensitive to defects thanks to specific arrangements in hydroxyapatite crystals [10]. Recent findings [11] suggest that both micro-scale toughening and weakening mechanisms could coexist inside the same bone region, highly depending from lacunar distribution and morphological characteristics.

Despite the enormous interest in identifying early signs of bone damage [12-14] and in elucidating eventual lacunar-level pathological alterations that result in premature bone deterioration, the characterization of the lacunar system remains difficult today due to its location embedded within the opaque, mineralized matrix and its intricate complexity. Conventional 2D imaging techniques such as light microscopy [15,16], scanning electron microscopy (SEM) [17], transmission electron microscopy [18], and atomic force microscopy [19] are often destructive and present several uncertainties because the slicing direction may bias the results due to missing information about the third dimension. To overcome this issue, various 3D imaging techniques are explored to shed light on the lacunar network physio-pathological characteristics [20]. Confocal laser scanning microscopy (CLSM) [21], multiplexed 3D-confocal imaging combining different fluorescent stains [22], serial focused ion beam SEM [23,24] allow to generate 3D reconstructions of bone micro-scale architectural features, but suffer from several limitations, including, as in the case of CLSM, spherical aberration, that impairs axial resolution in depth [23,24]. Computed micro-tomography (micro-CT) represents a powerful tool for acquiring lacunar level scans while keeping sample integrity [25-28]; however, this technique lacks in phase contrast for micro-cracks recognition. Synchrotron radiation, with sufficiently high photon flux and coherent beam properties, in combination with in-situ mechanical testing appears as a prominent solution to capture the existent cross-talks between the lacunar network and occurring crack mechanisms at an unprecedently high resolution [29].

Even if 3D imaging techniques are able to provide volumetric information and investigate the 3D bone micro-architectural and structural properties with a non-destructive approach, human bone data remain scarce and are generally limited to a very small field of view [30]. On that basis, a complete morphological analysis of osteocyte lacunae would be of primary interest, since related alterations appear to have an effect on bone remodeling process [31]. Preliminary findings obtained specifically via in situ synchrotron imaging suggest that there exists a specific correlation between osteocyte lacunar morphology/distribution changes and physio-pathological processes. Osteocyte lacunar density seems to decrease with age [32-37], together with a reduction in size, and in presence of bone diseases (such as osteoarthritis) [38]. Lacunar sphericity, directly linked to the osteocyte capability to sense the surrounding tissue strain, appear to increase with age and in pathological conditions, i.e. osteoporosis [11]. Therefore, it becomes more and more evident how changes in the lacunae and perilacunar bone tissue properties could be an early warning sign of altered osteocyte mechanosensitivity and consequently of pathology.

Nowadays, an additional high impact wake-up call to shed deeper light on this correlation rises from the outbreak of Covid-19 pandemic: a slowdown in the bone formation processes is hypothesized as a direct outcome of the virus infection, which, together with the increased sedentary lifestyle of the bedridden hospitalized patients, lead to a reduction in bone mass and strength [39-41]. Indeed, recent disruptive preliminary studies [42] focus on the interaction between the virus and Angiotensin-converting enzyme (ACE2). ACE2 is a receptor for the spike glycoprotein of the Covid-19 and it is expressed by osteoclasts and osteoblasts. When Covid-19 targets to ACE2, this enzyme expression appears to be downregulated, resulting in an unbalanced bone homeostasis, and an alteration in the lacuno-canalicular network and signaling pathways. If this hypothesis would be confirmed, Covid-19 disease and long-Covid phenomena could have a tremendous effect on bone micro-scale architecture deterioration, leading to macro-scale critical fracture [43,44].

However, despite the enormous potentialities of 3D imaging techniques combined with finite element analyses, these approaches are limited by the low number of osteocyte lacunae that can be studied per sample, due to the massive computational costs linked to the 3D processing. This issue is mainly preventing a large-scale validation of ground-breaking scientific theories that elevate lacunar morphological and densitometric variations as the key for elucidating pathological alterations.

Recently, a novel artificial intelligence (AI)-based tool for automatic large-scale osteocyte lacunar detection and investigation, based on image-guided failure assessment (IGFA), becomes accessible [45]. The power and rigor of the method in mapping lacunar distribution in the 3D trabecular space are validated in human bone samples.

Thanks to this methodical approach, the present study aims, for the first time, at: (1) elucidating the existent cross-talks between lacunar shape and density in presence of different load distributions, as particularly evident in the femoral head where bone structure is arranged as a response to the external loading scenario; (2) quantifying the effect of lacunar-level alterations on crack initiation and propagation mechanisms via the aid of multi-scale finite element strategies; (3) quantifying micro-scale effects of the osteoporotic disease; (4) offering ground-breaking insights in long-term Covid effects on bone health.

Here, we consider 180 female healthy, 180 female osteoporotic, 180 female Covid-19 and 180 male Covid-19 samples harvested from femoral heads after hip replacement surgery. Synchrotron IGFA is applied to a total of 60 samples harvested from the proximal, medial and distal zone of the femoral head with respect to the pelvis.

2. Materials and methods

2.1. Patient recruitment and clinical assessment

Human femoral heads (FH) are collected with prior authorization from the Ethics Committee (approval date: 13/05/2020,

ClinicalTrials.gov ID: NCT04787679) of San Raffaele Hospital (Milan, Italy) and signed approval consent of the patients. The rationale of sample site choice specifically resides in determining whether there exists a relationship between lacunar shape and density in presence of different load distributions. Indeed, while at the *meso*-scale it is widely recognized [46,47] that trabeculae are arranged in the three-dimensional space as a response to the external loading scenario (Wolff's law), the micro-scale architectural adaptation to mechanical loadings is still a black box.

Three populations are considered in this study: osteoporotic, Covid-19 and a healthy control group.

Patients over eighteen years old are recruited if they met the following criteria: (a) have undergone primary hip replacement; (b) have a routine preoperative CT scan. Exclusion criteria includes: (a) bone disease (non-osteoporotic) such as to invalidate sample analysis, including but not limited to genetic disorders and bone tumors; (b) patients with contralateral hip replacement and/or other synthetic bone substitutes/fixation devices in the contralateral hip; (c) Patients with synthetic bone substitutes/fixation devices in the hip of interest.

Clinical parameters, inclusive of age, are reported in Table 1, that includes a power analysis too. While considered patients share approximately the same age, therefore no statistically significant difference is detected for this parameter, $p < 0.05$ is identified in the BV/TV parameter, that is a measure of the *meso*-scale deterioration of trabecular structures, particularly evident in osteoporotic subjects. The T-score, defined are the standard deviation of patient's bone density (undergoing DXA examination) compared with a statistical sample of 25–30 years old white women, is evaluated in agreement with the World Health Organization (WHO) guidelines. Therefore, a T-score $\leq$ -2.5 corresponds to an osteoporotic subject.

As concerns Covid-affected patients, they have received, in accordance to WHO, a diagnosis of SARS-CoV-2 virus made by a positive antigenic or molecular swab. The clinical picture varies from patient to patient and the experienced symptoms are detected at different levels, including the respiratory, cardiovascular, gastrointestinal trait and even the psychological sphere. All recruited patients are symptomatic with a positive swab within 12 months prior to the hip replacement surgery.

As pertains healthy and osteoporotic group, only females are included in the study, while in the Covid-affected population we consider both males and females in a balanced proportion (Table 1).

2.2. Bone sample collection and preparation

36 trabecular samples are obtained from each FH by cutting it along the principal tensile and compressive stress trajectories. Samples are classified in accordance to their distance from the pelvis as P (proximal), M (medial) and D (distal). The cut segments are then fixed in formaldehyde [48-50] to avoid any bacteria contamination, stored in 70% ethanol, and embedded into epoxy resin endcaps. Samples are then kept wet in isotonic saline prior to mechanical testing and during the experimental procedure.

Bone samples have a square cross-section of 16 mm^2 and a total height of 14 mm. Three samples (one P, one M and one D) for each FH undergone IGFA inside the synchrotron, the remainders are subjected to mechanical testing outside the synchrotron.

2.3. In situ image-guided failure assessment (IGFA)

The mechanical testing phase of human bone samples is conducted both outside and inside the synchrotron via an *ad hoc* Micro-Compression Device (MCD). The device, described in detail in [51], is characterized by high maneuverability, due to its limited weight (<0.75 kg) and height (<115 mm). We use a compact stepper motor as linear actuator (NA23C60; Zaber Technologies Inc., Vancouver, CA), ensuring the possibility to reach 400 N [52], while for the load control, we exploited a precision miniature load cell (Model 34, Honeywell Sensing & Control, Columbus, OH, USA). Bone samples are kept hydrated in a buffer saline solution during the entire testing phase. The external cylinder and the internal bone sample housing system made of polymethyl methacrylate (PMMA, Young Modulus (E) = 3300 MPa [53]) guarantee both human eye and X-ray transparency, that are helpful in double checking specimen correct positioning. Bone samples, after an initial 2–3 N preload, are tested under displacement control. Each compression step is performed with a step amplitude of 0.1 mm, a displacement rate of 0.1 mm/s and is followed by 3 min of relaxation time during which the imposed displacement is maintained (see Fig. 1). The instantaneous load measured by the cell is recorded with a sampling frequency of 10 Hz and plotted in real time allowing them to be continuously monitored during the test. With the aim of capturing the cross-talks between lacunar arrangements and micro-crack propagation, we design a specific alternance of tomographic acquisitions and micro-compression steps. This allows to capture crack evolution, starting from its nucleation, propagation and final failure of the sample.

IGFA is performed in the experimental hutch of the SYRMEP beamline (Elettra synchrotron, Trieste, Italy), as described in detail in [11]. Briefly, experiments are carried out using the white beam configuration in propagation-based phase-contrast modality with a sample-to-detector distance of 150 mm, and an X-ray energy of 25.6 keV obtained with a Silicon foil 1.5 mm thick. Projections are recorded with a camera based on a 16-bit, water-cooled Orca Flash 4.0 sCMOS detector (2048 $\times$ 2048 pixels) coupled to a 17 μm-thick GGG scintillator screen. The synchrotron scans are performed according to the so-called half acquisition mode (i.e., an off-center rotation over 360°, in order to almost double the width of the field-of-view) [54], according to the following parameters: pixel size = 1.6 μm, exposure time = 0.1 s, number of projections = 1800, field of view = 3.28 · 3.28 mm. The scan is performed in fly mode, indeed the MCD continuously rotates on the platform to which is rigidly coupled, during the acquisition; for each scan one flat field image (without the sample) and one dark field image (without X-ray illumination) are taken. With the adopted syn-

Table 1
Clinical information of recruited patients. Data are shown with mean ± standard deviation. In the right column the power analysis is reported. Bold text indicates $p < 0.05$. [a] p in Kruskal-Wallis H tests. [b] p in Chi-squared test. [c] p in Mann-Whitney *U* test.

Groups	Healthy	Osteoporotic	Covid-19	p-value
Number of patients [/]	5	5	10	
Age [years]	74.4 ± 3.2	77.5 ± 5.1	75.1 ± 4.3	p = 0.324 [a]
Sex [female/male]	5/0	5/0	5/5	**p = 0.036**[b]
T-score	/	−3.22 ± 0.78	/	
BV/TV [%]	36.12 ± 1.07	28.31 ± 1.23	34.78 ± 1.27 (females) 35.78 ± 2.12 (males)	**p < 0.001** [a] p (Covid male-Covid female) = **0.0013**[c]

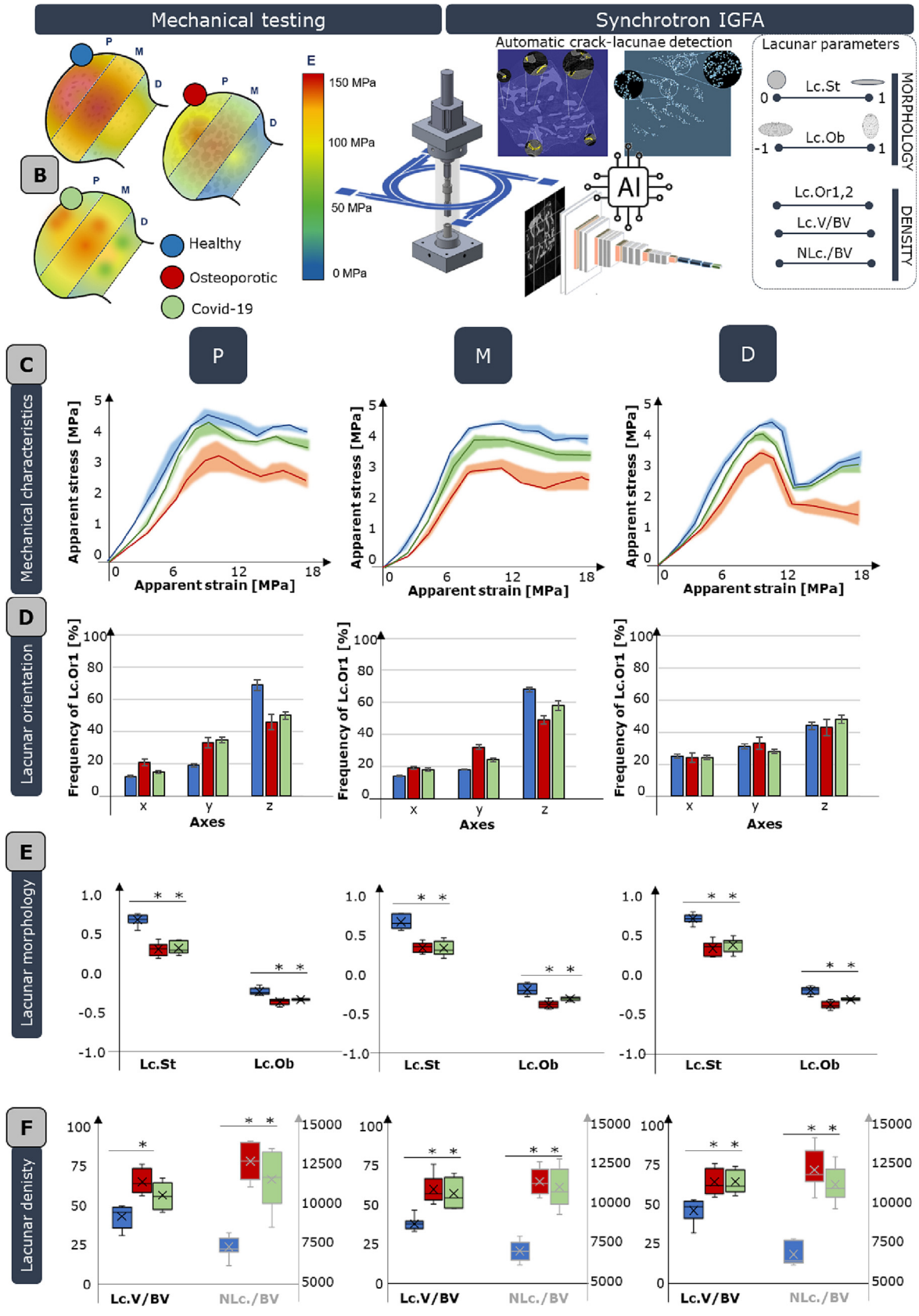
Mechanical testing
Synchrotron IGFA
Automatic crack-lacunae detection
Lacunar parameters
B
P
M
D
E
150 MPa
100 MPa
50 MPa
0 MPa
Healthy
Osteoporotic
Covid-19
AI
Lc.St
Lc.Ob
Lc.Or1,2
Lc.V/BV
NLc./BV
MORPHOLOGY
DENSITY
C
Mechanical characteristics
Apparent stress [MPa]
Apparent strain [MPa]
D
Lacunar orientation
Frequency of Lc.Or1 [%]
Axes
E
Lacunar morphology
F
Lacunar denisty

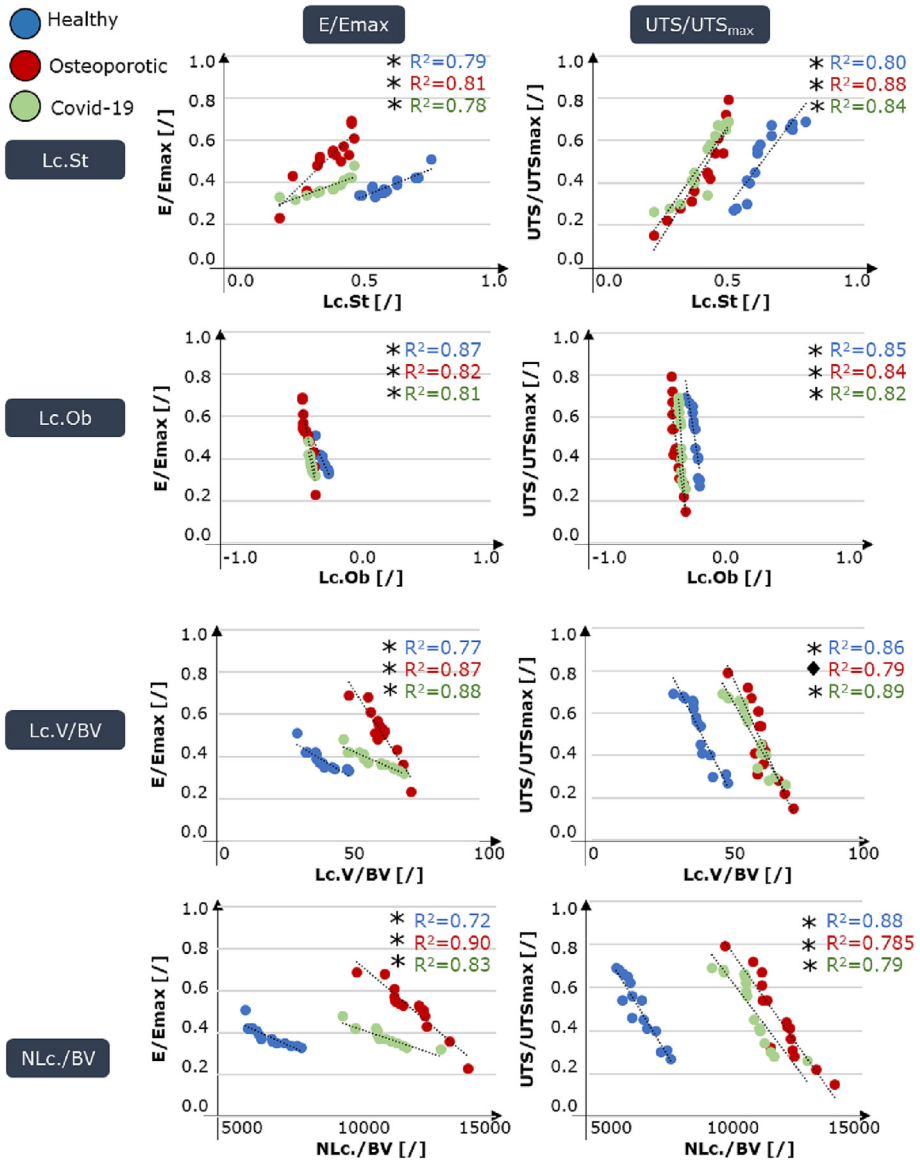

Fig. 2. Correlation between osteocyte lacunar morpho-densitometric features and *meso*-scale mechanical characteristics of the samples tested inside the synchrotron, including normalized Young modulus and normalized ultimate tensile stress. The scatter plots include best fitted lines and related R-square for each physio-pathological condition. *p-values < 0.001, ◆ p-value < 0.05.

chrotron scanning parameters, the input radiation dose on the sample imposed by synchrotron radiation corresponds to 165 Gy. In literature, it is reported that for bone material a safe level is between 30 kGy and 35 kGy, while material properties are significantly changed above 70 kGy [55-57]. Additionally, research works conducted by the authors [11,45] with the same experimental setup and synchrotron radiation parameters evidenced that the mechanical properties in terms of E of the scanned samples are within the values detected in the respective femoral head during mechanical tests outside the synchrotron; thus, validating further considerations on scanned samples.

Fig. 1. Meso- and micro-scale bone characteristics in dependence of external loading scenario. **A.** harvesting site, i.e. femoral heads, and the complexity of femur multi-scale architecture. At the macro-scale (on the left), the loading distribution is reported (JRF: joint reaction force, F_{abd}: force due to the abductor muscles, F_{ip}: force due to the iliopsoas muscle, F_{vl}: force due to vastus lateralis muscle). At the *meso*-scale, trabeculae are arranged along principal tensile and compressive groups of fibers. At the micro-scale, lacunae are the sites where osteocyte reside. **B.** testing equipment, comprising an ad hoc micro-compression device and synchrotron in situ imaging. This allows to map the average Young modulus inside healthy (blue dot), osteoporotic (red dot) and Covid-19 (green dot) femoral heads (on the left). On the right, an artificial intelligence-based tool, specifically a convolutional neural network is exploited for the automatic segmentation of micro-cracks and lacunae, which morpho-densitometric parameters are visually schematized (including: Lacunar Stretch, Lc.St., Lacunar Oblateness, Lc.Ob., Lacunar Orientation 1 and 2, Lc.Or1,2, lacunar volume density, Lc.V/BV, and lacunar number density, NLc./BV). **C.** Meso-scale mechanical curves of healthy, osteoporotic and Covid-19 femoral heads are reported in terms of apparent stress-apparent strain and clustered with respect to the harvesting region (proximal, P, medial, M and distal, D). Standard deviations of data are reported in a lighter shade. **D.** lacunar orientation of the three physio-pathological conditions with respect to the ×, y and z (loading direction) axis of the sample and the harvesting region. **E.** lacunar morphological parameters including stretch and oblateness. **F.** lacunar densitometric parameters, including lacunar volume and lacunar number with respect to the bone volume. Boxplots are shown with mean, median, lower and upper quantile and whiskers. * p-value < 0.05. (For interpretation of the references to colour in this figure legend, the reader is referred to the web version of this article.)

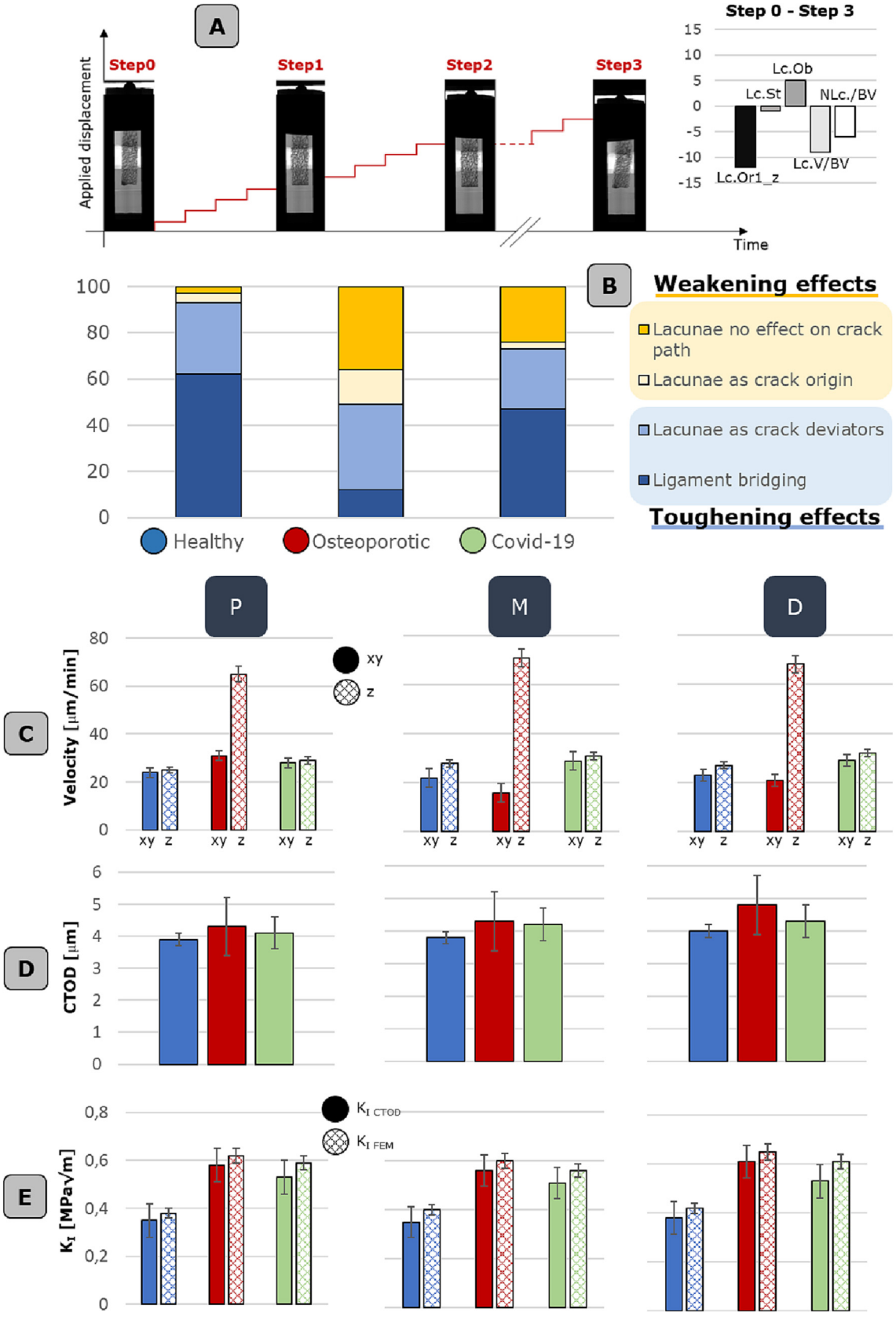
A
Step0
Step1
Step2
Step3
Applied displacement
Time
Step 0 - Step 3
Lc.Ob
Lc.St
NLc./BV
Lc.V/BV
Lc.Or1_z
B
Weakening effects
Lacunae no effect on crack path
Lacunae as crack origin
Toughening effects
Lacunae as crack deviators
Ligament bridging
Healthy
Osteoporotic
Covid-19
P
M
D
C
Velocity [μm/min]
xy
z
D
CTOD [μm]
E
K_I [MPa√m]
$K_{I\ CTOD}$
$K_{I\ FEM}$

Projections are pre-processed by a single-distance phase-retrieval algorithm [58] with a δ/β parameter (i.e., ratio between the real and imaginary parts of the material refraction index given by n = 1 - δ - i β) = 20 ± 1, selected for a good visualization of crack and lacunae details. The reconstruction is then performed using the conventional filtered back projection algorithm available in the SYRMEP Tomo Project (STP) v1.4, that is an open-source software used and implemented at the SYRMEP beamline [59]. A Matlab code, described in detail in [11], removes artifacts and noises that could appear in the inter-trabecular voids.

2.4. Image post-processing using AI

A Convolutional Neural Network (CNN) is implemented for automatic crack and lacunar detection, based on the Keras VGG16 built-in model [60]. This artificial intelligence (AI)-based tool has been previously validated in [45]; with the baseline setup, networks achieve>0.99 level of accuracy for both cracks and lacunae, and>0.87 of the mean Intersection over Union (meanIoU) adopted as validation metric. This approach is particularly encouraging for the development of powerful recognition system to comprehend the cross-relationships that exist between micro-architectural features (such as osteocyte lacunae) and micro-damages. The method is particularly suitable, being computationally efficient with little memory requirement and suitable for problems that are large in terms of data/parameters [61].

2.5. Lacunar densitometric and morphological analysis

Lacunar analyses are performed by processing the 3D reconstructions obtained from the CNN automatic lacunar detection in the full bone sample. The maximum and minimum lacunar volume limits are chosen as 300 voxels (corresponding to about 1229 μm^3) and 98 voxels (corresponding to about 400 μm^3), respectively. Threshold range are selected with respect to previous morpho-densitometric [25] and histological [62] studies on human lacunae. Both morphological [63] and densitometric lacunar parameters are considered for the analysis. Morphological parameters are based on the shape tensor, which describes the shape and orientation of a single lacuna with respect to its center of volume. Diagonalizing the symmetric tensor, it is possible to obtain the eigenvectors and the corresponding eigenvalues linked to the lacunae. We define the Lacuna Stretch (Lc.St) as the ratio between the largest and the smallest eigenvalue difference and the largest eigenvalue. Lacunar stretch could vary from 0 to 1, where 0 corresponds to a perfectly spherical lacuna, and 1 to an infinitely stretched one. Lacunar oblateness (Lc.Ob) quantifies the geometrical shape of a lacuna, with values between −1 and 1, with −1 corresponding to a perfect prolate rod, and 1 corresponding to a perfect oblate plate. Lacuna Orientation (Lc.Or), instead, quantifies the directions of the two larger lacunar semi-axes; indeed, Lc.Or1 refers to the direction of the longest semi-axis, while Lc.Or2 is the second longest semi-axis. In prolate lacunae, only Lc.Or1 has meaningful implications, while in the presence of an oblate lacuna, both orientations should be considered. In addition to morphological parameters, densitometric lacunar parameters include the lacunar volume density (Lc.V/BV), corresponding to the volume fraction of trabeculae occupied by lacunae, and the lacunar number density (NLc./BV), that gives a quantitative correlation between the number of lacunae and the extent of analyzed bone portion.

2.6. Crack fracture-mechanics based analysis

As pertains micro-cracks analysis, we exploited a fracture-mechanics based framework. CNN-based automatic detection on 2D slices and the further 3D reconstruction allow for measuring: crack length, crack propagation velocity, and crack-tip opening displacement (CTOD). Crack length is measured with a scale set to 1 pixel = 1.6 μm. Crack propagation velocity ($v = \frac{\Delta a_{step(n)-step(n-1)}}{\Delta t_{step(n)-step(n-1)}}$) is computed by measuring crack length in two subsequent tomographic acquisitions, where Δa is the difference in length (or height) of the same crack between two subsequent steps, and Δt is the interval of time corresponding to the applied displacement at two different levels. The CTOD allows to estimate the separation of the crack faces near the tip and is directly measured from synchrotron images. From the CTOD we extrapolate the corresponding toughness values (K_{CTOD}) with the approximated equation $K_{CTOD} \approx \sqrt{CTOD * E * \sigma_y}$, where E is the Young modulus and σ_y is the yielding strength of the sample material, derived from the mechanical tests conducted inside the synchrotron.

2.7. Numerical modeling

Multi-scale numerical models are exploited to quantify the stress-field alterations due to the presence of different lacunar networks and to evaluate the interactions between propagating cracks and alterations in the lacunar morphology/density.

The output images have all the same dimension and are imported in software Fiji-ImageJ; BoneJ plugin [14] is applied to obtain a.STL file to be imported in Abaqus (a 32 to 8-bit downscale is applied to the whole bone model in order to reduce the computational costs). Shrink wrap hexaedral mesh is adopted in Hypermesh software to capture local multi-scale heterogeneities [13] with an element size of 7.5-pixels for the global model. In Abaqus a linear elastic simulation is performed reproducing the experimental setup, imposing a fixed support at the bottom surface and a displacement of 0.4 mm at the top one, which corresponds to the first compression step. The simplification of adopting a linear elastic numerical strategy, while preventing from modeling the full mechanical response of bone after trabecular collapse, has several advantages [11,64], including: i) simplicity: Linear elastic models are computationally efficient, making them well-suited for modeling bone structures up to the micro-scale; ii) validity for small deformations: Linear elastic models are valid for small deformations, which is often sufficient for modeling bone structures. Small deformations can occur during normal daily activities and are well within the linear range of bone's mechanical behavior; iii) Flexibility: Linear elastic models can be easily adapted to different bone geometries, making them a versatile tool for studying bone mechanics both at the meso- and micro-scale. The material

Fig. 3. Lacunar morpho-densitometric feature effects on micro-damage occurrence **A.** Synchrotron image-guided failure assessment conducted at four different stages: i.e., uncompressed state (named step 0), after four applied displacement levels of 0.1 mm (step 1), after additional four applied displacement levels of 1 mm (step 2) and at the complete failure of the sample (step 3). The radiographs of an exemplificative sample are reported for each step. At step 3, the femoral head bone sample is fully collapsed. The differences in lacunar morpho-densitometric parameters between Step0 and Step 3 are reported on the right. **B.** Quantification of toughening and weakening effects occurring at the micro-scale in all three physio-pathological conditions. In > 60% of the healthy cases is detected the presence of ligament bridging. **C.** Micro-crack velocity along xy plane and z direction, corresponding to the applied displacement. **D.** Crack-tip opening displacement (CTOD) values. **E.** Stress intensity factor, K_I, values extrapolated from the quantification of the CTOD and from the finite element analysis. All values indicated in **C**, **D** and **E** are reported for all the three physio-pathological conditions, considering P, M, D zone. Histograms are reported with data standard deviation bars.

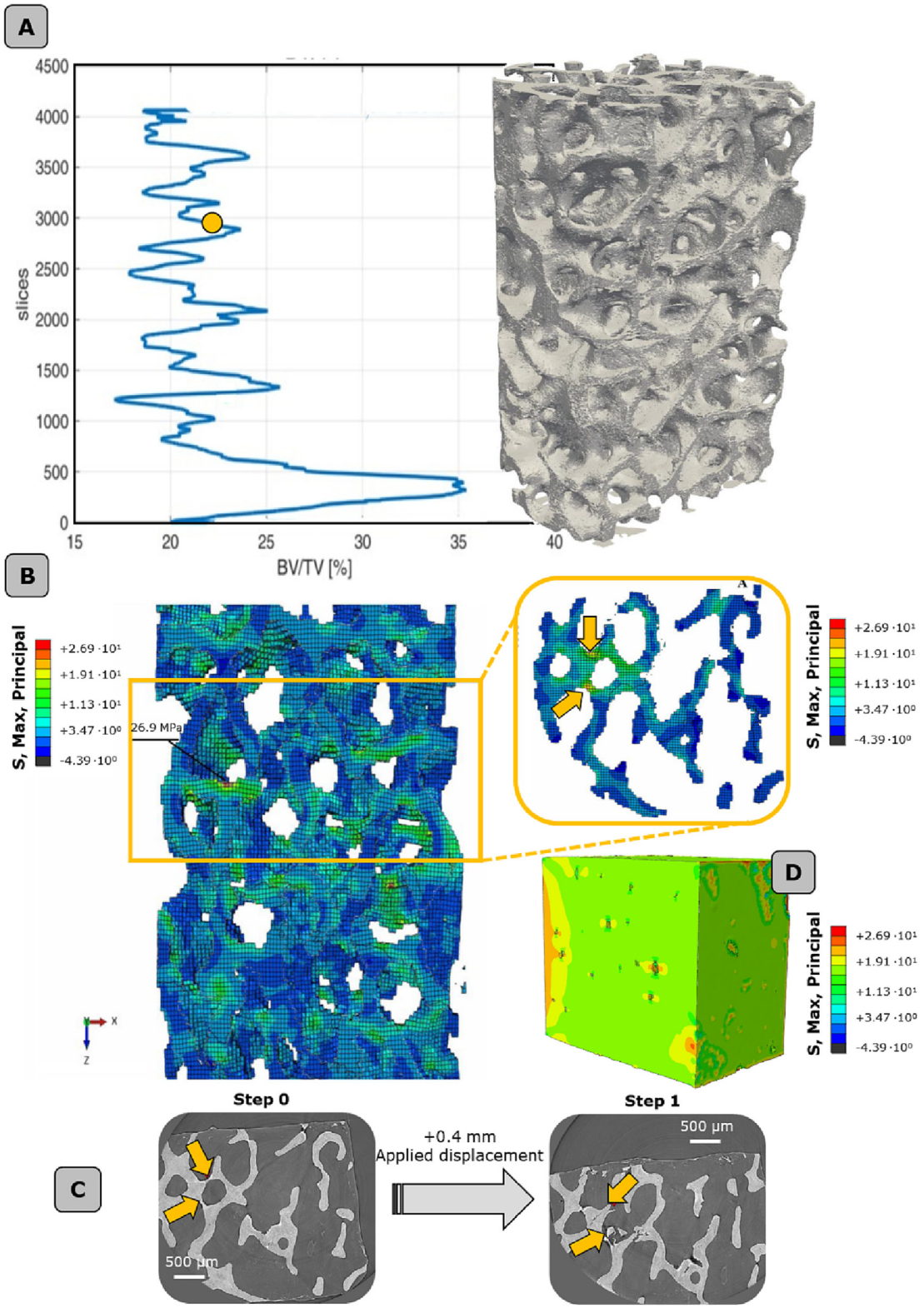

Fig. 4. Multi-scale numerical modeling of trabecular bone. **A.** full bone (global level) and indication of the Bone volume ratio (BV/TV). The yellow dot indicates the critical zone where average low values of BV/TV are detected. **B.** localization of the failure band, in the proximity of the maximum principal stresses region. **C.** localization of the most stressed/strained trabecula and validation of the models with synchrotron images at increasing applied displacement levels. **D.** evaluation of the stress state at the lacunar level by means of a finite element model in the most stressed region of the failure band. (For interpretation of the references to colour in this figure legend, the reader is referred to the web version of this article.)

input for the bone are Young's modulus, derived from experimental tests and adjusted in accordance to Schaffler [62], and Poisson's ratio of 0.3. The failure band model is characterized by 1.28 mm height and a refined mesh of pixel size equal to 3. The lacunar level model is performed with a pixel size of 1 and derives its boundary conditions from the respective failure band model.

From the numerical models, values of stress intensity factor, K_I, are extrapolated using the LEFM equation ($K_I = \beta * \sigma * \sqrt{\pi * a}$), where σ represents the stress normal to the crack present in the trabecula. $\beta \approx 1.12$ is the shape function of a surface crack (a necessary approximation given the complexity of the problem and recurrent crack branching phenomena [65]).

2.8. Statistics

Output data obtained from experimental analyses are processed with the software Minitab. An initial statistical analysis is carried out using the Shapiro-Wilk normality test, in order to verify whether or not the data have a normal distribution. Statistically significant differences among data samples are analyzed considering their distribution. Normally distributed data are compared using parametric tests: 2 Sample *t*-test is used when only two populations are compared, while ANOVA is implemented for three or more populations. Non-normally distributed data are analyzed using the non-parametric Mann-Whitney test (for comparison between two populations of data) or Kruskal-Wallis (for comparison among three populations of data). P values below 0.05 are retained statistically significant. For parameters with $P < 0.05$ in Kruskal Wallis H test, post hoc analysis adopting Dunn test with Bonferroni correction is performed. As concerns the power analysis in Table 1, Chi-squared test is exploited too, in order to compare the observed frequencies of two or more groups (frequency of male/female in healthy, osteoporotic and Covid-19 group) with the expected frequencies. As pertains correlations between micro-scale morpho-densitometric parameters and *meso*-scale mechanical characteristics, scatter plots include best fitted lines and related R-square for each physio-pathological condition.

3. Results

3.1. Lacunar network morpho-densitometric features effects on bone strength

To assess whether bone multi-scale architectural features affect bone strength, 36 samples from each femoral heads (FH) are harvested following the direction of the trabeculae (Fig. 1A) and tested under compression with an in house designed MCD (Fig. 1B). Among them, three samples from each FH are selected for IGFA inside the synchrotron.

The chosen anatomical site (Fig. 1A) is characterized by a multi-scale complexity: at the macro-scale it is the region where mechanical loads are transmitted from the pelvis through the cotyloid cavity, at the *meso*-scale trabeculae are arranged in the three-dimensional space along principal compressive and tensile groups. As a result, morpho-densitometric characteristics of femoral trabeculae adapt and optimize themselves to various loads acting on the hip joint. Consequently, the intrinsic femoral mechanical properties could show high inter-subject and intra-subject variability, in agreement with Wolff's mechano-biological theory [66], evidencing an adaptation to the physio-pathological loading scenario. This *meso*-scale variability is deeply explored in all samples coming from female FH by evaluating the Young modulus (E), ultimate tensile strength (UTS), yield strength and ultimate strain in the proximal (P), medial (M) and distal (D) zone with respect to the pelvis. The P regions of all the 15 analyzed femoral heads (Fig. 1C) display higher values of Young's modulus (E = 126 ± 24 M Pa, average value for all FH) where the predominant principal compressive group directly sustains the loads transmitted from the acetabulum (a mapping of average E values is reported in Fig. 1B, on the left). The D region, characterized by few trabecular bundles, appears less stiff, with Young's modulus in the range of 71 ± 12 MPa (average value for all FH), significantly lower ($p < 0.05$) than the P zone (Fig. 1B, on the left). No statistically significant difference is detected between E values of P and M in both healthy, osteoporotic and Covid FH, respectively; this could be explained by looking at the anatomical conformation of M zone, exactly at the interception of the two main compressive and tensile groups, resulting in an excellent ability to sustain the applied compressive displacement too. Significant variability is detected in the E values of the P regions, and it is more evident for all mechanical parameters in the osteoporotic condition (Fig. 1C). Indeed, not only the Young modulus, but the ultimate stress, ultimate strain and yield strength are highly variable in the osteoporotic cases (as further detailed in paragraph 3.3 and Fig. 5B). As pertains Covid-19 cases, no statistically significant difference is detected in the *meso*-scale mechanical properties if compared to healthy cases; a huge variability is detected in the intra-population YS values (Fig. 6B), specifically in the P region.

Moving to the micro-scale, with the aim of assessing eventual correlations between lacunar characteristics and mechanical response to external loads, an AI-based tool is exploited (Fig. 1B, on the right). A convolutional neural network, which accuracy is demonstrated in [45], allows for automatic lacunar detection, permitting the processing of million lacunae simultaneously. Identified features cover the micro-porosities three dimensional orientation (Lc.Or1, that corresponds to the main lacunar semi-axis) (Fig. 1 D), morphological (lacunar stretch, Lc.St, and lacunar oblateness, Lc.Ob) and densitometric (lacunar volume, Lc.V/BV, and number of lacunae, NLc./BV, normalized by the bone volume) characteristics (Fig. 1E,F). Lacunar orientation does not show a unique trend: the orientation of the main lacunar semi-axis is predominantly (frequency > 60% in the proximal and medial zone, frequency > 40% in the distal zone) in the z plane for healthy samples (Fig. 1D), so the one parallel to the loading direction. As concerns osteoporotic subjects (Fig. 1D, in red), lacunae are more evenly distributed, specifically in the D region, with a slight increase (+9 ± 0.2%) of Lc.Or1 in the xy plane with respect to the P and M zones. As concerns lacunar morphological parameters (Fig. 1 E), Lc.St does not show significant variations within P, M, D regions, appearing more linked to the health status. Indeed, statistically significant differences are found when comparing healthy, osteoporotic and Covid-19 populations in terms of both Lc.St and Lc.Ob. Further details are provided in section 3.3 and 3.4. Same considerations could be derived from the analysis of lacunar densitometric parameters; indeed, no significant differences are detected within P, M, D zones and the shown variations are attributed to the pathological conditions. Both lacunar volume and lacunar number density present slight internal variability (∼5%) within the same FH. The difference in Lc.V/BV and NLc./BV is proven larger (∼42%) when comparing the physiological to the two pathological conditions with respect to the intrinsic FH variability. However, even if a wide number of lacunae is considered, the number of samples scanned at the synchrotron is three for each FH, pending for prudent observations when providing correlations to the physio-pathological state.

To detect whether micro-scale characteristics are a reflection of the *meso*-scale mechanical behavior, we report (Fig. 2) the correlations between normalized mechanical characteristics (we reported statistically significant correlations in terms of E/Emax and US/UTSmax) and lacunar-level parameters. Lc.St is positively correlated with the normalized Young modulus ($R^2 > 0.79$); an analogous trend is visible for the correlation between the stretch and the normalized ultimate tensile strain ($R^2 > 0.80$) for all the analyzed samples (Fig. 2). Oblateness appears negatively correlated ($R^2 > 0.81$) with both normalized E and UTS, demonstrating that

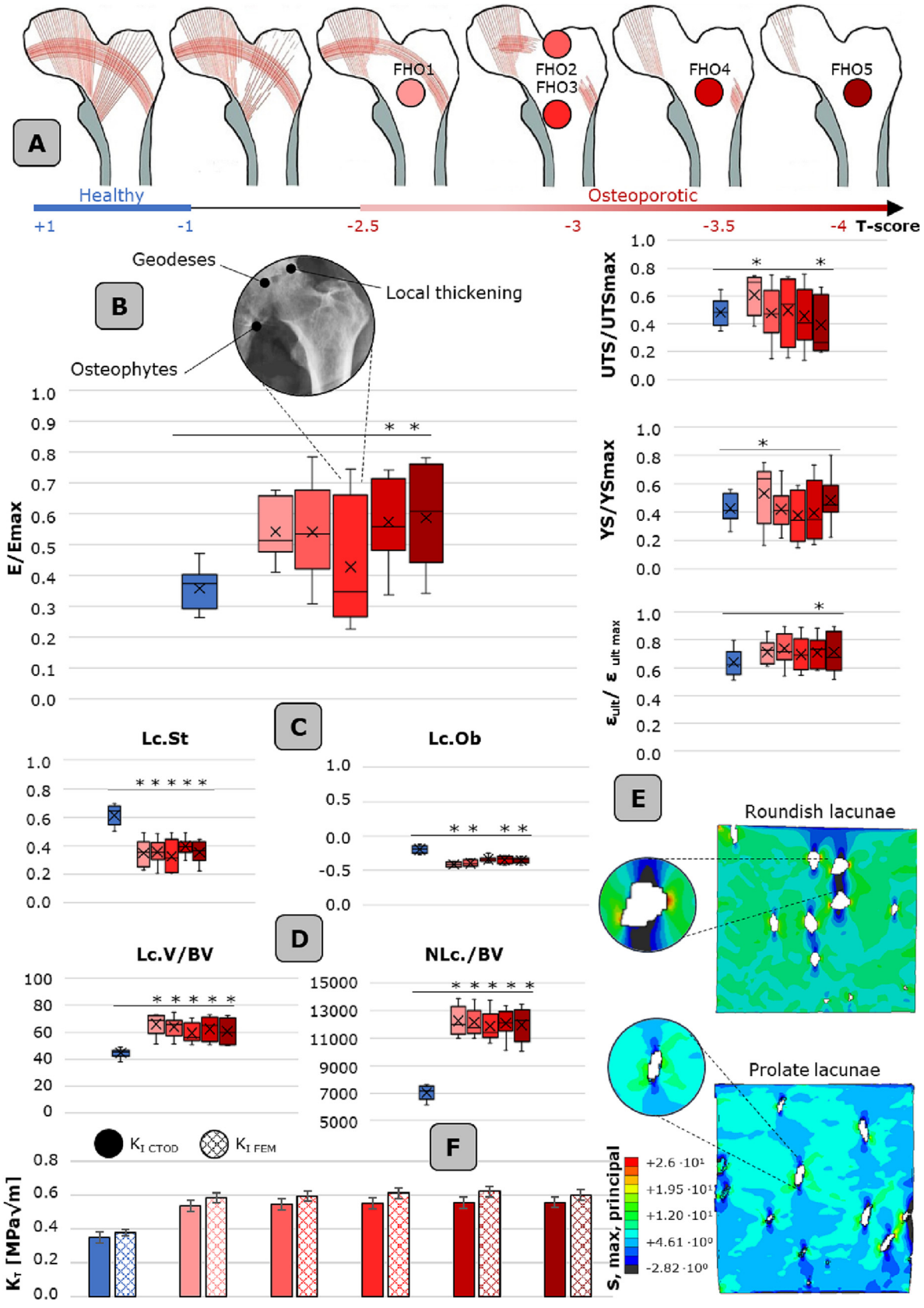
A
FHO1
FHO2
FHO3
FHO4
FHO5
Healthy
Osteoporotic
+1
-1
-2.5
-3
-3.5
-4
T-score
B
Geodeses
Local thickening
Osteophytes
E/Emax
UTS/UTSmax
YS/YSmax
εult/ εult max
C
Lc.St
Lc.Ob
D
Lc.V/BV
NLc./BV
E
Roundish lacunae
Prolate lacunae
S, max, principal
+2.6 ·10¹
+1.95 ·10¹
+1.20 ·10¹
+4.61 ·10⁰
-2.82 ·10⁰
F
KI CTOD
KI FEM
KT [MPa√m]

a more prolate condition is a synonym of higher mechanical response. Same negative correlation is evidenced for all densitometric parameters.

3.2. Lacunar network morpho-densitometric features effects on micro-cracks initiation and propagation

The adopted synchrotron IGFA approach is the key for investigating and quantifying eventual cross-talks between lacunar features and micro-crack initiation and propagation mechanisms. Indeed, three samples for each FH are tested and scanned at increased applied displacement. Step 0 corresponds to the scan in the uncompressed state, in steps 1 and 2 a displacement of 0.4 mm is gradually applied per step to the sample. The final step 3 aims at capturing bone failure, when additional 0.8 mm displacement is applied before the last tomographic acquisition (Fig. 3A).

Firstly, potential alterations of lacunar morpho-densitometric features due to mechanical testing are checked (Fig. 3A, on the right). It is worth highlighting that no local remodeling is expected, since bone is excised from human donors and is preserved in formaldehyde, preventing any osteoblasts/osteoclasts/osteocytes survival. Statistically significant differences in volume are detected only in Step 3 ($p < 0.05$) with respect to the uncompressed Step 0; this could be explained by observing typical Step 3 synchrotron slices, where micro-scale damages coalesce into *meso*-scale cracks that cross the entire trabecula, totally altering the original lacunar network arrangement. Same trend appears for all the densitometric parameters; the reduced number of lacunae in Step 3 is uniquely related to the sample failure into separate fragments. A slight increase in oblateness is found across Step 1–2-3 (+5% in total), though no specific trend in stretch behavior can be recognized. Therefore, there is a tendency for lacunae to become oblate when compressed; this finding is in accordance with the orientation, indicating an increased preferential orientation through the steps in the directions orthogonal to the applied displacement.

With the aim of evaluating the interplays between cracks and lacunae, the implemented CNN for the automatic crack detection results as a promising tool for the 3D analysis of damage phenomena starting from 1.6 μm resolution synchrotron slices. Indeed, 2D observations deriving from bidimensional slices are often limited when looking for micro-scale toughening and weakening phenomena. From a preliminary bidimensional recognition of micro-porosities and propagating cracks at increased applied displacement, lacunae appear as frequent crack deviators (Fig. 3B), slowing down its progression in>31% of healthy samples, 26% of Covid-affected cases and 37% of osteoporotic population. In line with a previous work [11], ligament bridging phenomenon, meaning the initiation of parallel not coalescent tiny cracks, occur in the majority (>62%) of the healthy control group, specifically in the samples harvested from the P region.

Moving to the AI-based 3D reconstruction, we exploit a fracture-mechanics based framework to quantify lacunar features effect on bone strength. Specifically, we evaluate crack propagation velocities (Fig. 3C) along x-y and z direction (corresponding to the perpendicular and parallel direction with respect to the applied compressive displacement respectively). No specific trend is found when comparing M, P, D samples neither for healthy nor for Covid cases, while a predominant z direction is highlighted for 89% of the osteoporotic samples. CTOD measures (Fig. 3D) appear within the same order of magnitude for all the samples, around 4.6 ± 1.2 μm. The CNN-based 3D reconstruction of the whole sample at the lacunar detail permits the implementation of multi-scale numerical models on the tested specimens, towards the quantification of the stress intensity factor, K_I, due to micro-scale heterogeneities (Fig. 3E).

At the *meso*-scale (Fig. 4 A, B), higher values of maximum principal stresses are mostly located in the region with the lowest BV/TV, coherently with the experimental findings that show local buckling phenomena occurring in the same zone (Fig. 4C). While trabecular arrangement plays a core role in determining the failure band, lacunar micro-porosities significantly alter the stress distribution (Fig. 4D). K_I values extrapolated from FEM analyses ($K_{I\,FEM}$) in the proximity of lacunae are in line with the K_{CTOD} calculated from experimental observations. K_I values for the two pathological conditions appear higher (∼+34%) than the healthy control group.

3.3. Lacunar morpho-densitometric alterations in presence of osteoporotic disease and consequences on multi-scale bone strength

The adopted methodological approach, including *meso*-scale mechanical testing and combining synchrotron IGFA with the power of artificial neural networks, allows to shed light on the physio-pathological response to applied loadings. At the *meso*-scale, we test 180 samples harvested from 5 osteoporotic femoral heads, equally distributed in P, M and D regions. In all considered FHs, an evident deterioration in both primary compressive and tensile group of trabecular bundles is diagnosed after hip replacement surgery (Fig. 5A). In just a single case, characterized by a T-score < -3 corresponding to severe osteoporosis, a degradation in secondary trabecular patterns is highlighted from clinical observation.

Concerning osteoporotic inter-patient's variability, all mechanical parameters are normalized with respect to the maximum value detected in the respective FH, as reported in Fig. 5B. This allows to neglect intrinsic variations in terms of donor age range or eventual comorbidities that may locally affect the morphological trabecular arrangement. The normalized Young modulus is characterized by high variability and is statistically significantly higher than the healthy counterpart ($p < 0.05$). The reported variability, visible in all mechanical parameters, is attributable to two factors: the presence of bone tissue thickening phenomena due to local arthrosis, or the evidence of bone cysts. These geodeses appear as pseudocystic cavitary formations with fibromyxoid content that generate in the subchondral bone of joints, altering local mechanical response. In terms of intra-patient variability, as anticipated in section 3.1, the P and M regions show significantly higher mechanical characteristics with respect to the D zone (Fig. 1C), as elucidated for healthy subjects, indicating that the transmission of loads continues to occur from the acetabular area to the femoral shaft gradually passing to the neck region.

To evaluate the effect of osteoporosis on morpho-densitometric lacunar parameters (Fig. 5C,D), all 15 osteoporotic samples are

Fig. 5. Osteoporosis effect of bone meso- and micro-scale morpho-mechanical characteristics. **A.** progressive deterioration of the principal and secondary tensile and compression group. The osteoporotic FH are reported with respect to their T-score. **B.** Mechanical characteristics (normalized with respect to the maximum value detected in each FH) of the osteoporotic FHs with respect to the healthy control group. Reported values are: E/Emax, UTS/UTSmax, YS/YSmax and εult/ εult_max. **C.** Lacunar morphological parameters and **D.** lacunar densitometric parameters of the osteoporotic FHs with respect to the healthy condition. **E.** computational models evidencing the stress state in presence of osteoporotic micro-porosities, i.e. roundish lacunae (upper model) and healthy, i.e. flattened prolate lacunae (bottom model). For these lacunar level models, boundary conditions are extrapolated from the global full bone model, as detailed in section 2.7. **F.** stress intensity factors calculated based on the crack-tip opening displacement (CTOD) and the finite element models for each osteoporotic FH and the healthy case. Boxplots are shown with mean, median, lower and upper quantile and whiskers. * p-value < 0.05. Histograms are reported with data standard deviation bars.

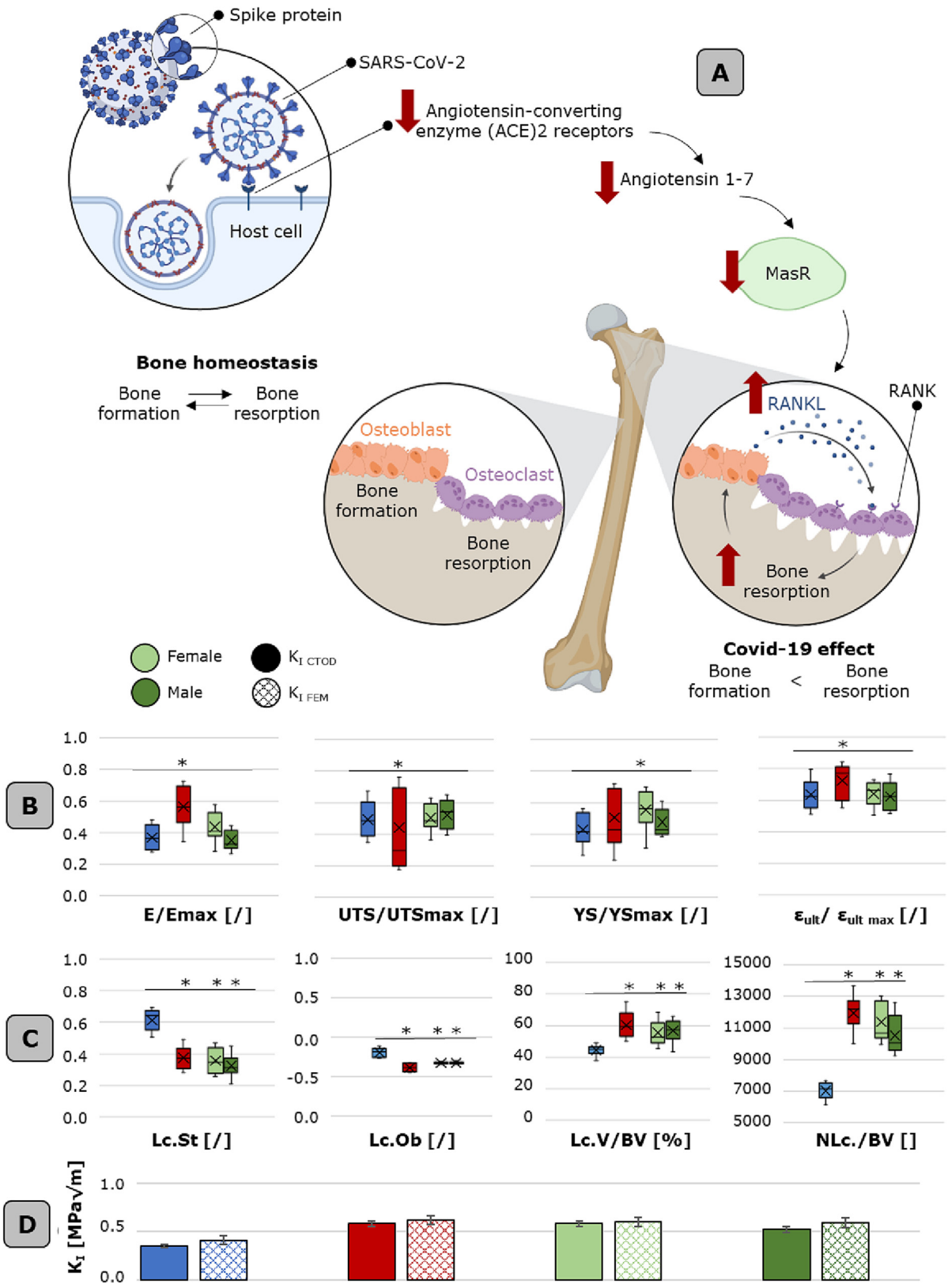

Fig. 6. Covid-19 effects on bone *meso*-and micro-scale morpho-mechanical characteristics. **A.** Schematic of Covid-19 hypothesized effects on bone remodeling mechanisms. Covi-19 targets angiotensin-converting enzyme (ACE2) receptor, producing a downregulation of Angiotensin 1–7/MasR cascade. ACE2 and MasR are expressed by osteoblasts and osteoclasts, meanwhile, the activation of ACE2/Ang-(1–7)/MasR axis reduce the bone resorptive milieu by inhibiting the expression of receptor activator of nuclear factor-kappaB ligand (RANKL). **B.** Meso-scale mechanical characteristics (normalized with respect to the maximum value detected in each FH) of both male and female Covid-19 FH, with respect to the healthy and osteoporotic cases. Reported values are: E/Emax, UTS/UTSmax, YS/YSmax and εult/ εult_max. **C.** Lacunar morphological parameters and lacunar densitometric parameters of the Covid-19 FHs with respect to the healthy/osteoporotic condition. **E.** stress intensity factor calculated based on the crack-tip opening displacement (CTOD) and the finite element models for Covid-19 FH and the healthy/osteoporotic cases. Boxplots are shown with mean, median, lower and upper quantile and whiskers. * p-value < 0.05. Histograms are reported with data standard deviation bars.

compared at the uncompressed state to the 15 healthy ones. Statistically significant differences are found in several lacunar parameters, i.e. lacunar stretch ($p < 0{,}001$), lacunar oblateness ($p < 0{,}001$) and lacunar volume ($p < 0{,}001$) when comparing the healthy to the osteoporotic case. The statistical significance is reached, permitting to assert that lacunae in the analyzed osteoporotic trabecular bones are larger, less stretched and less oblate than in the healthy counterpart. Lacunar density parameters are also investigated, turning to the assertion that the tested osteoporotic FHs have a larger lacunar volume and number density compared to the non-osteoporotic ones ($p < 0.001$). These findings suggest that the most critical difference between osteoporotic and non-osteoporotic cases is the large dimensions and roundish shape of lacunae that can be found in the former, rather than any specific orientation of the micro-porosities.

As expected, these morpho-densitometric alterations produce an effect on bone strength, not only at the *meso*-scale (as reported in section 3.1), but at the micro-scale too, generating different stress distributions and concentration sites. In Fig. 5E we compare two exemplificative lacunar-level models, characterized by more roundish (Fig. 5E, upper part) and more flattened and prolate lacunae (Fig. 5E, bottom part), asserting that spherical lacunae significantly alter the stress field, rather than the healthy flattened counterpart. Lacunae play also a role in crack initiation and propagation phenomena, as demonstrated in the evaluation of K_I. $K_{I\ FEM}$ and $K_{I\ CTOD}$, while being comparable and guaranteeing the validity of the implemented models, permit to assert that osteoporotic lacunar network generates significantly higher stress intensity factor sites ($p < 0.05$) than healthy subjects, resulting in local failures that generate the whole sample collapse.

3.4. Covid-19 and the bone: An underestimated multi-scale cross-relationship

The promising results obtained in assessing the intimate mechanobiological links between micro-scale porosities and damage in osteoporotic patients, open the doors to an unprecedent investigation. Indeed, clinical hypotheses correlating the short and long term Covid-19 effects on bone architecture (Fig. 6A) are still not yet validated, due to limitations in large scale micro-analysis of bone complex structure. The adopted methodological strategy, proven effective in automatic segmentation of million lacunae and cracks is the key for shedding light on eventual alterations on bone multi-scale structure due to the pandemic.

To increase sample size, we harvested 5 FHs from female patients and 5 FHs from male subjects and we test under compression a total of 360 samples.

At the *meso*-scale, if we compare 5 healthy and 5 female Covid FHs (Fig. 6B), no statistically significant difference is detected in the normalized Young modulus of the two populations, displaying slightly higher values ($\sim$ +4.6%) in the Covid case. Covid-affected FHs are characterized by higher variability, specifically in E/Emax and UTS/UTS max. The same trend is detected for all the considered mechanical parameters. As concerns the comparison between the 5 male and 5 female FHs (Fig. 6B), statistically significant values ($p < 0.05$) are reported for E/Emax, which is lower (E/Emax = 0.38 ± 0.13) in the case of males. Not a uniform trend could be displayed for other mechanical parameters.

Considering micro-scale investigation, impressive results are obtained from the morpho-densitometric analyses of the lacunar network (Fig. 6C). The most relevant observation is linked to the analysis of Lc.St: it appears that statistically significant differences ($p < 0.001$) are exhibited by Lc.St between the healthy and Covid-19 groups. Indeed, lacunae appear more roundish and spherical, as it is demonstrated for the osteoporotic group. The results also indicate that osteoporotic and Covid-19 lacunae share similar increase in volume and number density, while being less oblated than the healthy control group. This is a particularly disruptive finding, since it demonstrates and support, for the first time, the hypothesis of alterations in the complex bone hierarchical architecture due to long-term Covid effects. The difference in Lc.V/BV and NLc./BV is proven larger ($\sim$29%) when comparing the Covid to the healthy condition with respect to the same Covid group variability. Indeed, lacunae in males appear larger and more flattened than the female counterpart, but high variability is detected in the considered parameters.

As pertains fracture mechanics parameters, crack propagation velocity doesn't show a statistically significant preferential direction, as occurs in the healthy state (Fig. 3C). CTOD values are much higher for the Covid-19 case than the healthy FH (4.7 ± 0.1 in the first case and 3.8 ± 0.2 in the second one). The exploitation of finite element multi-scale strategies permits the evaluation of stress intensity factor sites, due to the presence of micro-scale heterogeneities. As an interesting outcome, $K_{I\ FEM}$ and $K_{I\ CTOD}$ outcomes (Fig. 6D) are not only within the same order of magnitude also for Covid sample models, but are close to the values obtained in the osteoporotic cases (percentage difference < 6%), with $K_{I\ FEM\ Covid}$ values being slightly lower than the osteoporotic ones.

4. Discussion

Our study exploits, for the first time, the power of in situ image-guided failure assessment combined with artificial intelligence-based strategies, to reveal novel insight in human trabecular bone micro-architectural adaptation to physio-pathological conditions. The over-arching aim of our work is to demonstrate four clinical hypotheses, that still lack of scientific validation: i) there exists an intrinsic variability in trabecular bone morpho-densitometric-mechanical features and this could be related to the external loading scenario; ii) micro-scale bone characteristics could alter fracture initiation and propagation mechanisms; iii) osteoporosis signs may start appearing at the micro-scale, correlated to alteration in osteocyte lacunar characteristics; iv) there exists an underestimated link between Covid-19 and bone micro-scale alterations due to long-term direct and indirect pandemic effect. To provide point by point validation to these theories, we select as anatomical site of interest the human femoral head, which fractures are among the most burdening in terms of hospitalization, long-term care and psycho-social side effects. For these reasons, the adoption of a micro-scale perspective could be the key to diagnose early signs of disease determined by alterations at the lacunar level and prevent the catastrophic evolution of micro-damages into macro-scale fractures.

Regarding the ***first clinical hypothesis***, we exploit a multi-scale strategy, combining mechanical tests conducted outside the synchrotron, in order to map the mechanical characteristics of the entire FH, and IGFA analyses at 1.6 μm resolution, to evaluate eventual cross-talks between the micro-scale architecture and the harvesting site (Fig. 1). At the *meso*-scale, mechanical tests conducted under compressive displacement control, result to be in line with previous studies [51,67-69], that hypothesized notable differences in the proximal femur structure and thus in its mechanical properties, specifically depending on the sample harvesting position. Indeed, our samples, harvested in the direction of principal compressive and tensile groups of trabecular bundles, show statistically significant differences in their mechanical response, even inside the same FH. The distal zone to the acetabular fossa shows lower value of Young modulus with respect to the neighboring medial and proximal region, where the majority of the load is transmitted from the pelvis. Interesting results are found when analyzing physio-pathological states: significantly higher values

of E/Emax are detected in all osteoporotic FHs (Fig. 5), demonstrating that the degeneration in the trabecular groups effectively translates in a degradation of the mechanical characteristics, as mentioned in literature studies [46]. Eventually, the higher variability in E values in osteoporotic P regions is directly linked to local thickening due to the coexistence of arthritic phenomena, that are more likely to occur in the proximity of load transmission zones as a response to the impaired trabecular pattern. No statistically significant difference is detected when comparing the healthy control to the Covid-19 group, which normalized Young modulus values are significantly ($p < 0.05$) lower than the osteoporotic population, while being higher (but $p > 0.05$) than the healthy group (Fig. 6). This means that at the *meso*-scale Covid-19 population does not show any critical trabecular deterioration, but the high variability evidenced in the Young modulus could be an early manifestation of local inhomogeneous trabecular redistribution.

At the micro-scale the determination of site-dependent characteristics and their correlation with mechanical response has been often impaired by the impressive number of lacunae to be processed, resulting in high computational costs. The exploitation of convolutional neural network, now extended for large scale assessment of crack and lacunae characteristics, results a powerful tool for automatic identification of micro-scale architectural features with an accuracy>99%, translating previous literature approaches conducted on bovine bones [70] to the recognition of human bone micro-architectural features. Globally, lacunar major axis in healthy subjects appear mainly oriented in the z direction, so the one corresponding to the applied displacement. An exception is represented by samples harvested from the distal region, which lacunae are more evenly distributed, with a predominance along the xy plane (Fig. 1). This change of orientation could effectively result in an unfavorable condition in terms of bone resistance to external loads, inducing local bending [6]. Intra-group variability is present as pertains both morphological and densitometric lacunar parameters, but is proven lower with respect to inter-group one, demonstrating that both osteoporosis and Covid-19 pathologies could play a role on micro-scale architectural features. The positive correlation (Fig. 2) with $R^2 > 0.78$ for all the three physio-pathological conditions of lacunar stretch with respect to the normalized Young modulus and the negative correlation obtained with the oblateness are a demonstration of the complex multi-scale cross-talks existing in bone hierarchical structure.

The adopted methodological approach provides interesting insights in validating the ***second clinical hypothesis***, that focuses on the correlations between micro-scale features and damage occurrence. Here, we check that morpho-densitometric lacunar characteristics alter the stress–strain field of the surrounding bone tissue. Indeed, the stress concentration factor change with a variation in the lacunar shape [71], and this could be easily demonstrated by the simplified bidimensional numerical model that we report in Fig. 5. We present two cases, corresponding to roundish lacunae, elliptical lacunae in the direction parallel to the applied displacement. The most favorable case in terms of stress concentration corresponds to the elliptical lacunae, parallel to the applied displacement, exhibiting a stretch close to zero, and this case is typical of healthy subjects.

Lacunae also affect crack initiation and propagation (Fig. 3), in different ways depending from their size and shape; here, we demonstrate that micro-porosities, specifically in healthy cases, could be arranged in the three-dimensional trabecular space to avoid crack coalescence in a *meso*-scale fracture (ligament bridging phenomena). On the contrary, in presence of thinner trabeculae, typical of osteoporotic subjects, cracks are more prone to cross the entire trabecula. While crack propagation velocities in ×, y, z are comparable in all three physio-pathological cases, statistically significant higher velocities are detected along z direction only for osteoporotic cases, as a result of the *meso*-scale differences, specifically in the thinner trabeculae and the lower BV/TV values that this group shows. Additionally, when deriving stress intensity factors from computational finite element models (Fig. 4), validated by experimental synchrotron analyses, we calculate that stress intensity factor in spherical lacunae ($K_{I\ FEM\ osteoporotic} = 0.6 \pm 0.02\ MPa\sqrt{m}$) is higher than the one shown by more ellipsoidal ones ($K_{I\ FEM\ healthy} = 0.4 \pm 0.03\ MPa\sqrt{m}$). Taylor et al. [72] presented findings of 1–5 MPa $\sqrt{m}$ for a considerable sample population covering a broad range of ages, including both young and elderly individuals. It is essential to note that age plays a significant role in the values of K, leading to lower values for elderly individuals, as seen in the studied case. Additionally, all samples analyzed were taken from patients who had undergone hip surgery after being diagnosed with bone disease or fracture, indicating that they were not in normal physiological conditions. It is also noteworthy that while literature [72] discusses values for cortical human bone, data for trabecular bone is limited due to its intrinsic complexity, leading to a reasonable assumption of lower K values in trabecular bone than in cortical bone.

This last finding gives us intriguing hints for addressing the ***third clinical hypothesis*** we aim at validating. Indeed, osteoporosis is here proven to alter the morpho-densitometric characteristics of the lacunar network, resulting in less flattened, more oblate and larger lacunae. From the morphological feature perspective, the presence of more spherical lacunae in patients with lower BV/TV implies a change in mechanical sensitivity of the lacunar conformation, and consequently on the embedded osteocyte. Indeed, as mentioned before (Fig. 5) and supported by previous works on porous inorganic materials [73], we estimate that hoop stresses in spherical geometries are approximately twice as high as those in prolate ellipsoids. This result is exactly in line with our complex three-dimensional models in which we considered the 3D distribution of maximum principal stresses in physio-pathological conditions, reaching to the conclusion that stress concentration in spherical lacunae is higher than the flattened case. This observation could be counterintuitive if we observe the mechanobiological side: indeed, previous studies [74-76] have demonstrated the beneficial effect of lacunar stress amplification and its relevance in the transduction of cell signaling pathways. So, why osteoporotic lacunae are more able to amplify mechanobiological signals with respect to the healthy counterpart? Recent biological theories, that are in support of our biomechanical findings, state that the osteocytes in osteoporotic bone are able to modulate lacunar shape in zones of lower BV/TV as a compensatory mechanism [77]. However, this could be effective only at early pathological stages, where the detrimental effect on principal compressive and tensile trabecular bundles is still at its infancy. It is worth pointing out that the obtained results in terms of increased lacunar sphericity in osteoporotic subjects are in line with other research works [33,62], demonstrating that lacunar stretch is reduced in presence of patients with lower BV/TV [27].

From the lacunar densitometric feature perspective, osteoporotic micro-porosities are characterized by larger lacunar volume and number density (Fig. 5) compared to the healthy control group ($p < 0.001$). Translating these findings to the cellular world, this is in accordance with the biological evidence that correlates osteoporosis to a reduced bone matrix production per cell, resulting in higher lacunar volume. It is worth mentioning that the state-of-the-art lacunar network in physio-pathological conditions is a complex research area which is currently still hotly discussed. As pertains age-related lacunar variations, several studies, while agreeing in a reduced osteocyte capability to sense variations in tissue strains in osteoporotic subjects [78], are still debating on the concurrent effects of age on the lacunar morpho-densitometric characteristics [33]. Indeed, Müller group

[25,26,79] evidence that lacunar density decreased in human with respect to age and also lacunar volume appear smaller than the younger control group, demonstrating that age reduces lacunar network functionality, also from a canalicular perspective. However, other authors [34] highlight that these findings are highly dependent on the specific bone and on the location within the bone. The population considered in our research is within the same age range ($p > 0.05$, see Table 1); therefore, we can state that the highlighted modifications in the lacunar network could be mainly associated to the pathological conditions. However, a wider sample set will be ultimately needed to prove eventual age-related effects on bone micro-scale features.

Encouraged by the sensitivity of our methodological strategies in detecting early signs of bone alterations, we give here crucial milestones to demonstrate the ***fourth clinical hypothesis***. At present, as detailed in the introduction, direct and indirect consequences of the pandemic appear to alter bone remodeling processes. While at the *meso*-scale trabecular level, no statistically significant differences are detected in Covid-affected bone mechanical characteristics with respect to the healthy control group, at the micro-scale lacunar morphological features show variations when compared to the physiological population (Fig. 6). It is worth highlighting that lacunar shapes appear as more roundish and oblate than the healthy counterpart, as detected in the osteoporotic condition. This finding, supported also by alterations in lacunar densitometric parameters analogous to the osteoporotic case, is of peculiar importance, demonstrating, for the first time, that the pandemic could have induced alterations in bone micro-architectural features [43,44,80]. Even if these modifications are still not perceivable at the *meso*-scale, a patient specific ad hoc monitoring of bone mass and strength in Covid-19 affected patients appears as highly recommended in the next future.

Thanks to this study, we demonstrate that underestimated bone micro-scale alterations and adaptations to external mechanical loadings could result as an early sign of pathology, both for the well-known osteoporotic condition and the novel post-pandemic scenario. The performed power analysis allows to confirm that the detected lacunar-level differences can be evidenced for the given cohort size and data scatter at a statistically significant power. In any case, expanding the sample size would be a concrete benefit for future study perspectives, especially in the context of investigating the long-term effects of Covid-19 on bone micro-architecture. One notable advantage is that it can increase the statistical power of the present study, leading to more precise results and a reduced likelihood of type II errors. Additionally, enlarging the sample size can help mitigate the impact of sampling bias, allowing for findings that are more representative of the broader population. When examining the long-term effects of Covid-19 on bone micro-architecture, a larger sample size can be particularly advantageous as it enables researchers to assess the heterogeneity of this effect across various subgroups. For example, different age groups, sexes, and comorbidities may exhibit varying degrees of bone damage, and a larger sample size can provide the necessary power to detect these differences. Such insights into the pathophysiology of Covid-19 and its impact on bone health can be highly valuable in developing effective treatments and preventative measures.

In this study, some limitations could be evidenced: firstly, this research does not consider the gray zone existent between healthy and osteoporotic group, i.e. osteopenic conditions. It would be worth verifying whether there exists a progressive variation in both mechanical and lacunar characteristic alteration by expanding sample harvesting procedure. Nevertheless, bone samples from mild to moderate osteopenia without surgery requirement cannot be collected due to ethical issue with this same harvesting approach. Secondly, a critical eye should always be kept in monitoring radiation damage in tested specimens. Indeed, the effects of radiation on bone can vary depending on several factors, including the type and intensity of radiation, the duration of exposure, and the individual's age and overall health [29,81,82]. While in the considered samples Young modulus values fall inside the respective reference interval for all the femoral heads, a continuous monitoring should be performed specifically in post-yield mechanical properties and correlations should be drawn extending patient age dataset. Thirdly, it is necessary to underline that Covid-19 pathology is characterized by a huge number of variants and a widespread clinical picture. A prudent approach should be adopted: actually, both direct (downregulation of ACE2 expression due to the infection and consequent unbalanced homeostasis) and indirect effects (increased sedentary lifestyle, hospitalization) of Covid-19 may have generated bone micro-structural deterioration [44] and it is extremely complex to isolate direct effects of the pandemic on the skeletal system. However, all these aspects are a consequence of the pandemic that still haven't been understood yet. Further studies at the cellular level are therefore needed to isolate the direct effects of Covid-19 on bone micro-structure, to highlight eventual difference in lacunar alterations among Covid-19 variants and to correlate them with patient symptom severity.

At present, all the discussed findings draw the diagnostical eye to the recognition of bone micro-alteration early signs, which could be the key for targeted prevention and treatment.

5. Conclusions

In summary, this work unravels that there exists a strong link between bone micro-scale level architectural alterations and early pathology occurrence. Four are the core findings obtained via combining in situ mechanical testing, synchrotron imaging at an unprecedent resolution and AI-based strategies for automatic bone lacunae and cracks detection: (1) bone characteristics are highly varying as mechanobiological response to the external load transmission. At the micro-scale, this results in a variability in lacunar orientation; (2) lacunar morpho-mechanical characteristics affect crack initiation and propagation mechanisms, altering local stress state; (3) osteoporotic lacunae appear larger, less flattened, and more oblate than the healthy control group, resulting in statistically significant increased stress intensity factors ($K_I = 0.6 \pm 0.02$ $MPa\sqrt{m}$); (4) Covid-19 plays an effect in on both lacunar morphological and densitometric features, resulting in osteoporotic-like alterations affecting micro-porosities.

6. Data availability

The data that support the findings of this study are available from the corresponding author upon reasonable request.

CRediT authorship contribution statement

Federica Buccino: Conceptualization, Data curation, Investigation, Validation, Writing – original draft. **Luigi Zagra:** Investigation, Resources. **Elena Longo:** Investigation, Validation. **Lorenzo D'Amico:** Investigation, Validation. **Giuseppe Banfi:** Conceptualization, Resources. **Filippo Berto:** Investigation, Methodology. **Giuliana Tromba:** Investigation, Resources, Methodology. **Laura Maria Vergani:** Conceptualization, Investigation, Methodology, Validation, Supervision, Writing – review & editing.

Data availability

Data will be made available on request.

Declaration of Competing Interest

The authors declare that they have no known competing financial interests or personal relationships that could have appeared to influence the work reported in this paper.

References

[1] H. Qing, L. Ardeshirpour, P. Divieti Pajevic, V. Dusevich, K. Jähn, S. Kato, J. Wysolmerski, L.F. Bonewald, Demonstration of osteocytic perilacunar/canalicular remodeling in mice during lactation, J. Bone Miner. Res. 27 (5) (2012) 1018–1029.

[2] D.P. Nicolella, D.E. Moravits, A.M. Gale, L.F. Bonewald, J. Lankford, Osteocyte lacunae tissue strain in cortical bone, J. Biomech. 39 (9) (2006) 1735–1743.

[3] F. Buccino, C. Colombo, L.M. Vergani, A Review on Multiscale Bone Damage: From the Clinical to the Research Perspective, Materials (Basel) 14 (5) (2021) 1240.

[4] R. Gauthier, M. Langer, H. Follet, C. Olivier, P.-J. Gouttenoire, L. Helfen, F. Rongiéras, D. Mitton, F. Peyrin, 3D micro structural analysis of human cortical bone in paired femoral diaphysis, femoral neck and radial diaphysis, J. Struct. Biol. 204 (2) (2018) 182–190.

[5] P. Varga, B. Hesse, M. Langer, S. Schrof, N. Männicke, H. Suhonen, A. Pacureanu, D. Pahr, F. Peyrin, K. Raum, Synchrotron X-ray phase nano-tomography-based analysis of the lacunar–canalicular network morphology and its relation to the strains experienced by osteocytes in situ as predicted by case-specific finite element analysis, Biomech. Model. Mechanobiol. 14 (2) (2015) 267–282.

[6] D.B. Burr, Stress concentrations and bone microdamage: John Currey's contributions to understanding the initiation and arrest of cracks in bone, Bone 127 (2019) 517–525.

[7] Kola S K, Begonia M T, Tiede-Lewis L A M, Laughrey L E, Dallas S L, Johnson M L and Ganesh T 2020 Osteocyte lacunar strain determination using multiscale finite element analysis *Bone Reports* **12** 100277.

[8] E.A. Zimmermann, B. Busse, R.O. Ritchie, The fracture mechanics of human bone: influence of disease and treatment, Bonekey Rep. 4 (2015) 743.

[9] Martelli S, Giorgi M, Dall' Ara E and Perilli E 2021 Damage tolerance and toughness of elderly human femora *Acta Biomater.* **123** 167–77.

[10] F. Libonati, A.K. Nair, L. Vergani, M.J. Buehler, Mechanics of collagen–hydroxyapatite model nanocomposites, Mech. Res. Commun. 58 (2014) 17–23.

[11] Buccino F, Bagherifard S, D'Amico L, Zagra L, Banfi G, Tromba G and Vergani L M 2022 Assessing the intimate mechanobiological link between human bone micro-scale trabecular architecture and micro-damages *Eng. Fract. Mech.* **270** 108582.

[12] F. Libonati, L. Vergani, Bone Toughness and Crack Propagation: An Experimental Study, Proc. Eng. 74 (2014) 464–467.

[13] Colombo C, Libonati F, Rinaudo L, Bellazzi M, Ulivieri F M and Vergani L 2019 A new finite element based parameter to predict bone fracture *PLoS One* **14**.

[14] F. Buccino, C. Colombo, D.H.L. Duarte, L. Rinaudo, F.M. Ulivieri, L.M. Vergani, 2D and 3D numerical models to evaluate trabecular bone damage, Med. Biol. Eng. Comput. 59 (10) (2021) 2139–2152.

[15] S. Qiu, D.S. Rao, S. Palnitkar, A.M. Parfitt, Differences in osteocyte and lacunar density between Black and White American women, Bone 38 (1) (2006) 130–135.

[16] B. Yu, A. Pacureanu, C. Olivier, P. Cloetens, F. Peyrin, Assessment of the human bone lacuno-canalicular network at the nanoscale and impact of spatial resolution, Sci. Rep. 10 (2020) 3.

[17] M. Sasaki, S. Kuroshima, Y. Aoki, N. Inaba, T. Sawase, Ultrastructural alterations of osteocyte morphology via loaded implants in rabbit tibiae, J. Biomech. 48 (15) (2015) 4130–4141.

[18] M.A. Rubin, I. Jasiuk, The TEM characterization of the lamellar structure of osteoporotic human trabecular bone, Micron 36 (7-8) (2005) 653–664.

[19] O.L. Katsamenis, H.M.H. Chong, O.G. Andriotis, P.J. Thurner, Load-bearing in cortical bone microstructure: Selective stiffening and heterogeneous strain distribution at the lamellar level, J. Mech. Behav. Biomed. Mater. 17 (2013) 152–165.

[20] P. Schneider, M. Meier, R. Wepf, R. Müller, Towards quantitative 3D imaging of the osteocyte lacuno-canalicular network, Bone 47 (5) (2010) 848–858.

[21] R. Genthial, E. Beaurepaire, M.C. Schanne-Klein, F. Peyrin, D. Farlay, C. Olivier, Y. Bala, G. Boivin, J.C. Vial, D. Débarre, A. Gourrier, Label-free imaging of bone multiscale porosity and interfaces using third-harmonic generation microscopy, Sci. Rep. 7 (2017).

[22] S.A. Kamel-ElSayed, L.A.M. Tiede-Lewis, Y. Lu, P.A. Veno, S.L. Dallas, Novel approaches for two and three dimensional multiplexed imaging of osteocytes, Bone 76 (2015) 129–140.

[23] P. Schneider, M. Meier, R. Wepf, R. Müller, Serial FIB/SEM imaging for quantitative 3D assessment of the osteocyte lacuno-canalicular network, Bone 49 (2) (2011) 304–311.

[24] E. Raguin, K. Rechav, R. Shahar, S. Weiner, Focused ion beam-SEM 3D analysis of mineralized osteonal bone: lamellae and cement sheath structures, Acta Biomaterialia 121 (2021) 497–513.

[25] Goff E, Buccino F, Bregoli C, McKinley J P, Aeppli B, Recker R R, Shane E, Cohen A, Kuhn G and Müller R 2021 Large-scale quantification of human osteocyte lacunar morphological biomarkers as assessed by ultra-high-resolution desktop micro-computed tomography *Bone* **152** 116094.

[26] K.G. Yang, E. Goff, K.-l. Cheng, G.A. Kuhn, Y. Wang, J.-Y. Cheng, Y. Qiu, R. Müller, W.-W. Lee, Abnormal morphological features of osteocyte lacunae in adolescent idiopathic scoliosis: A large-scale assessment by ultra-high-resolution micro-computed tomography, Bone 166 (2023) 116594.

[27] Goff E, Cohen A, Shane E, Recker R R, Kuhn G and Müller R 2022 Large-scale osteocyte lacunar morphological analysis of transiliac bone in normal and osteoporotic premenopausal women *Bone* **160** 116424.

[28] Mirzaali M J, Libonati F, Ferrario D, Rinaudo L, Messina C, Ulivieri F M, Cesana B M, Strano M and Vergani L 2018 Determinants of bone damage: An ex-vivo study on porcine vertebrae ed D Vashishth *PLoS One* **13** e0202210.

[29] M. Mastrogiacomo, G. Campi, R. Cancedda, A. Cedola, Synchrotron radiation techniques boost the research in bone tissue engineering, Acta Biomater. 89 (2019) 33–46.

[30] G. Bevill, T.M. Keaveny, Trabecular bone strength predictions using finite element analysis of micro-scale images at limited spatial resolution, Bone 44 (4) (2009) 579–584.

[31] S. Blouin, B.M. Misof, M. Mähr, N. Fratzl-Zelman, P. Roschger, S. Lueger, P. Messmer, P. Keplinger, F. Rauch, F.H. Glorieux, A. Berzlanovich, G.M. Gruber, P. C. Brugger, E. Shane, R.R. Recker, J. Zwerina, M.A. Hartmann, Osteocyte lacunae in transiliac bone biopsy samples across life span, Acta Biomater. 157 (2023) 275–287.

[32] A.M. Ashique, L.S. Hart, C.D.L. Thomas, J.G. Clement, P. Pivonka, Y. Carter, D.D. Mousseau, D.M.L. Cooper, Lacunar-canalicular network in femoral cortical bone is reduced in aged women and is predominantly due to a loss of canalicular porosity, Bone Rep. 7 (2017) 9–16.

[33] Y. Carter, C.D.L. Thomas, J.G. Clement, D.M.L. Cooper, Femoral osteocyte lacunar density, volume and morphology in women across the lifespan, J. Struct. Biol. 183 (3) (2013) 519–526.

[34] L.M. Tiede-Lewis, S.L. Dallas, Changes in the Osteocyte Lacunocanalicular Network with Aging, Bone 122 (2019) 101–113.

[35] Y. Carter, C.D.L. Thomas, J.G. Clement, A.G. Peele, K. Hannah, D.M.L. Cooper, Variation in osteocyte lacunar morphology and density in the human femur — a synchrotron radiation micro-CT study, Bone 52 (1) (2013) 126–132.

[36] P. Milovanovic, B. Busse, Inter-site Variability of the Human Osteocyte Lacunar Network: Implications for Bone Quality, Curr. Osteoporos. Rep. 17 (3) (2019) 105–115.

[37] F.a. Liu, K.e. Hu, L.H. Al-Qudsy, L.-Q. Wu, Z. Wang, H.-Y. Xu, H. Yang, P.-F. Yang, Aging exacerbates the morphological and mechanical response of mineralized collagen fibrils in murine cortical bone to disuse, Acta Biomater. 152 (2022) 345–354.

[38] Sang W and Ural A 2022 Quantifying how altered lacunar morphology and perilacunar tissue properties influence local mechanical environment of osteocyte lacunae using finite element modeling *J. Mech. Behav. Biomed. Mater.* **135** 105433.

[39] L. McMichan, M. Dick, D.A. Skelton, S.F.M. Chastin, N. Owen, D.W. Dunstan, W. D. Fraser, J.C.Y. Tang, C.A. Greig, S. Agyapong-Badu, A. Mavroeidi, Sedentary behaviour and bone health in older adults: a systematic review, Osteoporos. Int. 32 (8) (2021) 1487–1497.

[40] Wang X, Wen Y, Xie X, Liu Y, Tan X, Cai Q, Zhang Y, Cheng L, Xu G, Zhang S, Wang H, Wei L, Tang X, Qi F, Zhao J, Yuan J, Liu L, Zhu P, Ginhoux F, Zhang S, Cheng T and Zhang Z 2021 Dysregulated hematopoiesis in bone marrow marks severe COVID-19 *Cell Discov. 2021 71* **7** 1–18.

[41] M. Tahtabasi, N. Kilicaslan, Y. Akin, E. Karaman, M. Gezer, Y.K. Icen, F. Sahiner, The Prognostic Value of Vertebral Bone Density on Chest CT in Hospitalized COVID-19 Patients, J. Clin. Densitom. 24 (4) (2021) 506–515.

[42] K. Zheng, W.C. Zhang, Y.Z. Xu, D.C. Geng, COVID-19 and the bone: underestimated to consider, Eur. Rev. Med. Pharmacol. Sci. 24 (2020) 10316–10318.

[43] L. Sapra, C. Saini, B. Garg, R. Gupta, B. Verma, P.K. Mishra, R.K. Srivastava, Long-term implications of COVID-19 on bone health: pathophysiology and therapeutics, Inflamm. Res. 71 (9) (2022) 1025–1040.

[44] W. Qiao, H.E. Lau, H. Xie, V.-M. Poon, C.-S. Chan, H. Chu, S. Yuan, T.-T. Yuen, K.-H. Chik, J.-L. Tsang, C.-Y. Chan, J.-P. Cai, C. Luo, K.-Y. Yuen, K.-C. Cheung, J.-W. Chan, K.-K. Yeung, Chan J F W and Yeung K W K 2022 SARS-CoV-2 infection induces inflammatory bone loss in golden Syrian hamsters, Nat Commun. 13 (1) (2022).

[45] Buccino F, Aiazzi I, Casto A, Liu B, Sbarra M C, Ziarelli G, Banfi G and Vergani L M 2023 The synergy of synchrotron imaging and convolutional neural networks towards the detection of human micro-scale bone architecture and damage *J. Mech. Behav. Biomed. Mater.* **137** 105576.

[46] J.Y. Rho, R.B. Ashman, C.H. Turner, Young's modulus of trabecular and cortical bone material: Ultrasonic and microtensile measurements, J. Biomech. 26 (2) (1993) 111–119.

[47] C. Sen, J. Prasad, Exploring conditions that make cortical bone geometry optimal for physiological loading, Biomech. Model. Mechanobiol. 18 (5) (2019) 1335–1349.

[48] E. Mick, H. Steinke, T. Wolfskämpf, J. Wieding, N. Hammer, M. Schulze, R. Souffrant, R. Bader, Influence of short-term fixation with mixed formalin or ethanol solution on the mechanical properties of human cortical bone, Curr. Dir. Biomed. Eng. 1 (2015) 335–339.

[49] F. Linde, H.C.F. Sørensen, The effect of different storage methods on the mechanical properties of trabecular bone, J. Biomech. 26 (10) (1993) 1249–1252.

[50] B. Kaye, C. Randall, D. Walsh, P. Hansma, The effects of freezing on the mechanical properties of bone, Open Bone J. 4 (2012) 14–19.

[51] F. Buccino, L. Zagra, P. Savadori, C. Colombo, G. Grossi, G. Banfi, L. Vergani, Mapping Local Mechanical Properties of Human Healthy and Osteoporotic Femoral Heads *SSRN Electron*, J. (2021).
[52] H. Sugita, M. Oka, J. Toguchida, T. Nakamura, T. Ueo, T. Hayami, Anisotropy of osteoporotic cancellous bone, Bone 24 (5) (1999) 513–516.
[53] B. Laboratories, Material Properties of Polystyrene and Poly(methyl methacrylate) (PMMA) Microspheres, Bangs Lab. Inc. (2015).
[54] T. Buzug, Computed tomography: From photon statistics to modern cone-beam CT, Comput. Tomogr. From Phot. Stat. to Mod. Cone-Beam CT (2008).
[55] S. Ma, O. Boughton, A. Karunaratne, A. Jin, J. Cobb, U. Hansen, R. Abel, Synchrotron Imaging Assessment of Bone Quality, Clinic Rev Bone Miner Metab 14 (3) (2016) 150–160.
[56] H.D. Barth, M.E. Launey, A.A. MacDowell, J.W. Ager, R.O. Ritchie, On the effect of X-ray irradiation on the deformation and fracture behavior of human cortical bone, Bone 46 (6) (2010) 1475–1485.
[57] H.D. Barth, E.A. Zimmermann, E. Schaible, S.Y. Tang, T. Alliston, R.O. Ritchie, Characterization of the effects of x-ray irradiation on the hierarchical structure and mechanical properties of human cortical bone, Biomaterials 32 (34) (2011) 8892–8904.
[58] D. Paganin, S.C. Mayo, T.E. Gureyev, P.R. Miller, S.W. Wilkins, Simultaneous phase and amplitude extraction from a single defocused image of a homogeneous object, J. Microsc. 206 (1) (2002) 33–40.
[59] F. Brun, S. Pacilè, A. Accardo, G. Kourousias, D. Dreossi, L. Mancini, G. Tromba, R. Pugliese, P. Dulio, A. Frosini, G. Rozenberg, Enhanced and Flexible Software Tools for X-ray Computed Tomography at the Italian Synchrotron Radiation Facility Elettra, Fundam Informaticae 141 (2-3) (2015) 233–243.
[60] Simonyan K and Zisserman A 2015 Very deep convolutional networks for large-scale image recognition *3rd Int. Conf. Learn. Represent. ICLR 2015 - Conf. Track Proc.*
[61] Kingma D P and Ba J L 2015 Adam: A method for stochastic optimization *3rd Int. Conf. Learn. Represent. ICLR 2015 - Conf. Track Proc.*
[62] B.R. McCreadie, S.J. Hollister, M.B. Schaffler, S.A. Goldstein, Osteocyte lacuna size and shape in women with and without osteoporotic fracture, J. Biomech. 37 (4) (2004) 563–572.
[63] K.S. Mader, P. Schneider, R. Müller, M. Stampanoni, A quantitative framework for the 3D characterization of the osteocyte lacunar system, Bone 57 (1) (2013) 142–154.
[64] T.M. Keaveny, X.E. Guo, E.F. Wachtel, T.A. McMahon, W.C. Hayes, Trabecular bone exhibits fully linear elastic behavior and yields at low strains, J. Biomech. 27 (9) (1994) 1127–1136.
[65] W.F. Hosford (Ed.), Mechanical Behavior of Materials, Cambridge University Press, 2005.
[66] H.M. Frost, Wolff's Law and bone's structural adaptations to mechanical usage: an overview for clinicians, Angle Orthod. 64 (1994) 175–188.
[67] A. Nazarian, J. Muller, D. Zurakowski, R. Müller, B.D. Snyder, Densitometric, morphometric and mechanical distributions in the human proximal femur, J. Biomech. 40 (11) (2007) 2573–2579.
[68] F. Linde, I. Hvid, N.C. Jensen, Material properties of cancellous bone in repetitive axial loading, Eng Med. 14 (4) (1985) 173–177.
[69] Spatafora G 2014 Optical Mechanical and Biochemical characterization of trabecular bone.
[70] Shen S C yun, Peña Fernández M, Tozzi G and Buehler M J 2021 Deep learning approach to assess damage mechanics of bone tissue *J. Mech. Behav. Biomed. Mater.* **123** 104761.
[71] Dowling N E 1999 Mechanical behavior of materials : engineering methods for deformation, fracture, and fatigue xviii, 830 p.
[72] D. Taylor, J.G. Hazenberg, T.C. Lee, Living with cracks: Damage and repair in human bone, Nat. Mater. 6 (4) (2007) 263–268.
[73] T. Davis, D. Healy, A. Bubeck, R. Walker, Stress concentrations around voids in three dimensions: The roots of failure, J. Struct. Geol. 102 (2017) 193–207.
[74] A. Rath Bonivtch, L.F. Bonewald, D.P. Nicolella, Tissue strain amplification at the osteocyte lacuna: A microstructural finite element analysis, J. Biomech. 40 (10) (2007) 2199–2206.
[75] A.R. Stern, D.P. Nicolella, Measurement and estimation of osteocyte mechanical strain, Bone 54 (2) (2013) 191–195.
[76] T.M. Skerry, L.E. Lanyon, L. Bitensky, J.o. Chayen, Early strain-related changes in enzyme activity in osteocytes following bone loading in vivo, J. Bone Miner. Res. 4 (5) (1989) 783–788.
[77] R.P. van Hove, P.A. Nolte, A. Vatsa, C.M. Semeins, P.L. Salmon, T.H. Smit, J. Klein-Nulend, Osteocyte morphology in human tibiae of different bone pathologies with different bone mineral density - Is there a role for mechanosensing?, Bone 45 (2) (2009) 321–329
[78] F. Donaldson, D. Ruffoni, P. Schneider, A. Levchuk, A. Zwahlen, P. Pankaj, R. Müller, Modeling microdamage behavior of cortical bone, Biomech. Model. Mechanobiol. 13 (6) (2014) 1227–1242.
[79] R. Voide, P. Schneider, M. Stauber, G.H. van Lenthe, M. Stampanoni, R. Müller, The importance of murine cortical bone microstructure for microcrack initiation and propagation, Bone 49 (6) (2011) 1186–1193.
[80] N. Napoli, A.L. Elderkin, D.P. Kiel, S. Khosla, Managing fragility fractures during the COVID-19 pandemic, Nat. Rev. Endocrinol. 16 (9) (2020) 467–468.
[81] M.M. Pendleton, S.R. Emerzian, J. Liu, S.Y. Tang, G.D. O'Connell, J.S. Alwood, T. M. Keaveny, Effects of ex vivo ionizing radiation on collagen structure and whole-bone mechanical properties of mouse vertebrae, Bone 128 (2019) 115043.
[82] Oliviero S, Giorgi M, Laud P J and Dall'Ara E 2019 Effect of repeated in vivo microCT imaging on the properties of the mouse tibia ed R K Roeder *PLoS One* **14** e0225127.